Progress In Electromagnetics Research, PIER 61, 159–192, 2006

INFRARED WAVE PROPAGATION IN A HELICAL WAVEGUIDE WITH INHOMOGENEOUS CROSS SECTION AND APPLICATION

Z. Menachem and M. Mond

Department of Mechanical Engineering
Ben-Gurion University of the Negev
Beer-Sheva 84105, Israel

Abstract—This paper presents an improved approach for the propagation of electromagnetic (EM) fields along a helical dielectric waveguide with a circular cross section. The main objective is to develop a mode model for infrared (IR) wave propagation along a helical waveguide, in order to provide a numerical tool for the calculation of the output fields, output power density and output power transmission for an arbitrary step's angle of the helix. Another objective is to apply the inhomogeneous cross section for a hollow waveguide. The derivation is based on Maxwell's equations. The longitudinal components of the fields are developed into the Fourier-Bessel series. The transverse components of the fields are expressed as functions of the longitudinal components in the Laplace plane and are obtained by using the inverse Laplace transform by the residue method. The separation of variables is obtained by using the orthogonal-relations. This model enables us to understand more precisely the influence of the step's angle and the radius of the cylinder of the helix on the output results. The output power transmission and output power density are improved by increasing the step's angle or the radius of the cylinder of the helix, especially in the cases of space curved waveguides. This mode model can be a useful tool to improve the output results in all the cases of the hollow helical waveguides (e.g., in medical and industrial regimes).

1. INTRODUCTION

Various methods for the analysis of cylindrical hollow metallic or metallic with inner dielectric coating waveguide have been studied in the literature [1–17]. A review of the hollow waveguide technology [1] and a review of IR transmitting, hollow waveguides, fibers and integrated optics [2] were published. The first theoretical analysis of the problem of hollow cylindrical bent waveguides was published by Marcatili and Schmeltzer [3]. Their theory considers the bending as a small disturbance and uses cylindrical coordinates to solve Maxwell equations. They derive the mode equations of the disturbed waveguide using the ratio of the inner radius r to the curvature radius R as a small parameter ($r/R \ll 1$). Their theory predicts that the bending has little influence on the attenuation of a hollow metallic waveguide. However, practical experiments have shown a large increase in the attenuation, even for a rather large R.

Marhic [4] proposed a mode-coupling analysis of the bending losses of circular metallic waveguide in the IR range for large bending radii. His study of nonsteady-state propagation improves the understanding of experimental procedures for the measurement of bending losses and provides practical limits to the rate of change of curvature consistent with single-mode propagation. In the circular guide it is found that the preferred TE_{01} mode can couple very effectively to the lossier TM_{11} mode when the guide undergoes a circular bend. The mode-coupling analysis [4] developed to study bending losses in microwave guides has been applied to IR metallic waveguides at $\lambda = 10.6\,\mu$m. For circular waveguides, the microwave approximation has been used for the index of refraction and the straight guide losses, and the results indicate very poor bending properties due to the near degeneracy of the TE_{01} and TM_{11} modes, thereby offering an explanation for the high losses observed in practice.

Miyagi et al. [5] suggested an improved solution, which provided agreement with the experimental results, but only for $r/R \ll 1$. A different approach [4, 6] treats the bending as a perturbation that couples the modes of a straight waveguide. That theory explains qualitatively the large difference between the metallic and metallic-dielectric bent waveguide attenuation. The reason for this difference is that in metallic waveguides the coupling between the TE and TM modes caused by the bending mixes modes with very low attenuation and modes with very high attenuation, whereas in metallic-dielectric waveguides, both the TE and TM modes have low attenuation. The EH and HE modes have similar properties and can be related to modes that have a large TM component.

Hollow waveguides with both metallic and dielectric internal layers were proposed to reduce the transmission losses. Hollow-core waveguides have two possibilities. The inner core materials have refractive indices greater than one (namely, leaky waveguides) or the inner wall material has a refractive index of less than one. A hollow waveguide can be made, in principle, from any flexible or rigid tube (plastic, glass, metal, etc.) if its inner hollow surface (the core) is covered by a metallic layer and a dielectric overlayer. This layer structure enables us to transmit both the TE and TM polarization with low attenuation [4, 6].

A method for the EM analysis of bent waveguides [7] is based on the expansion of the bend mode in modes of the straight waveguides, including the modes under the cutoff. A different approach to calculate the bending losses in curved dielectric waveguides [8] is based on the well-known conformal transformation of the index profile and on vectorial eigenmode expansion combined with perfectly matched layer boundary conditions to accurately model radiation losses. Light propagation through inhomogeneous media whose refractive index has weak changes with cylindrical symmetry around the propagation axis was published in [9], and two approximations based on geometric optics were examined. The cylindrical TEM_{00} and TEM_{10} laser modes were considered, and explicit analytical expressions for the light rays and intensity profiles for short and long times were derived. An improved ray model for simulating the transmission of laser radiation through a metallic or metallic dielectric multibent hollow cylindrical waveguide was proposed in [10, 11]. It was shown theoretically and proved experimentally that the transmission of CO_2 radiation is possible even through bent waveguide.

The propagation of EM waves in a loss-free inhomogeneous hollow conducting waveguide with a circular cross section and uniform plane curvature of the longitudinal axis was considered in [12]. For small curvature the field equations can, however, be solved by means of an analytical approximation method. In this approximation the curvature of the axis of the waveguide was considered as a disturbance of the straight circular cylinder, and the perturbed torus field was expanded in eigenfunctions of the unperturbed problem. Using the Rayleigh-Schrodinger perturbation theory, eigenvalues and eigenfunctions containing first-order correction terms were derived. An extensive survey of the related literature can be found especially in the book on EM waves and curved structures [13]. The radiation from curved open structures is mainly considered by using a perturbation approach, that is by treating the curvature as a small perturbation of the straight configuration. The perturbative approach is not entirely

suitable for the analysis of relatively sharp bends, such as those required in integrated optics and especially short millimeter waves. An analytical method to study a general helix-loaded structure has been published in [14]. The inhomogeneously-loaded helix enclosed in a cylindrical waveguide operating in the fast-wave regime. The tape-helix model has been used which takes into account the effect of the space-harmonics, and is used particularly in the cases that the structure is operated at high voltages and for high helix pitch angles. The propagation characteristics of an elliptical step-index fiber with a conducting helical winding on the core-cladding boundary [15] are investigated analytically where the coordinate systems are chosen for the circular and elliptical fibers. In their waveguides the core and the cladding regions are assumed to have constant real refractive indices n_1 and n_2, where $n_1 > n_2$. The fibers are referred to as the elliptical helically cladded fiber and the circular helically cladded fiber.

The models based on the perturbation theory consider the bending as a perturbation ($r/R \ll 1$), and solve problems only for a large radius of curvature. An improved approach has been derived for the propagation of EM field along a toroidal dielectric waveguide with a circular cross-section [16]. The derivation is based on Maxwell's equations for the computation of the EM field and the radiation power density at each point during propagation along a toroidal waveguide, with a radial dielectric profile. That method [16] employs toroidal coordinates (and not cylindrical coordinates, such as in the methods that considered the bending as a perturbation ($r/R \ll 1$)). In addition, terms up to fourth order in $1/R$ were considered in which the further orders are equal to zero.

The main objective of this paper is to generalize the numerical mode model [16] from a toroidal dielectric waveguide (approximately a plane curve) with a circular cross-section to a helical waveguide (a space curved waveguide for an arbitrary value of the step's angle of the helix) with a circular cross-section. Another objective is to demonstrate the ability of the model to solve practical problems with inhomogeneous cross-section in the case of a hollow waveguide. The generalized mode model with the two above objectives provides us a numerical tool for the calculation of the output fields and output power transmission for an arbitrary step's angle of the helix (δ_p). The results of this model are applied to the study of hollow waveguides with space curved shapes that are suitable for transmitting IR radiation, especially CO_2 laser radiation. In this paper we supposed that the modes excited at the input of the waveguide by the conventional CO_2 laser IR radiation ($\lambda = 10.6\,\mu$m) are closer to the TEM polarization of the laser radiation. The TEM_{00} mode is the fundamental and the

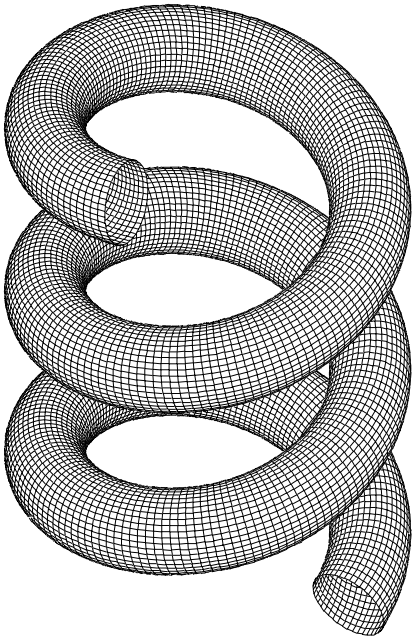

Figure 1. The circular helical waveguide.

most important mode. This means that a cross-section of the beam has a Gaussian intensity distribution. The output power transmission is improved by increasing the step's angle or the radius of the cylinder of the helix, especially in the cases of space curved waveguides.

2. FORMULATION OF THE PROBLEM

The method presented in [16] is generalized to provide a numerical tool for the calculation of the output transverse fields and power density in a helical waveguide (see Fig. 1), for an arbitrary value of the step's angle of the helix (δ_p). Fig. 1 shows the geometry of the helical waveguide with a circular cross section. The direction of the IR wave propagation is along the axis of the helical waveguide. The axis of the helical waveguide is shown in Fig. 2. The deployment of the helix and the step's angle δ_p are shown in Fig. 3. We start by finding the metric coefficients from the helical transformation of the coordinates. The latters will be used in the wave equations as will be outlined in the next section.

The helical transformation of the coordinates is achieved by two

rotations and one translation, and is given in the form:

$$\begin{pmatrix} X \\ Y \\ Z \end{pmatrix} = \begin{pmatrix} \cos(\phi_c) & -\sin(\phi_c) & 0 \\ \sin(\phi_c) & \cos(\phi_c) & 0 \\ 0 & 0 & 1 \end{pmatrix} \begin{pmatrix} 1 & 0 & 0 \\ 0 & \cos(\delta_p) & -\sin(\delta_p) \\ 0 & \sin(\delta_p) & \cos(\delta_p) \end{pmatrix}$$

$$\begin{pmatrix} r\sin\theta \\ 0 \\ r\cos\theta \end{pmatrix} + \begin{pmatrix} R\cos(\phi_c) \\ R\sin(\phi_c) \\ \zeta\sin(\delta_p) \end{pmatrix}, \qquad (1a, b, c)$$

where ζ is the coordinate along the helix axis, R is the radius of the cylinder, δ_p is the step's angle of the helix (see Figs. 2–3), and $\phi_c = (\zeta\cos(\delta_p))/R$. Likewise, $0 \leq r \leq a + \delta_m$, where $2a$ is the internal diameter of the cross-section of the helical waveguide, δ_m is the thickness of the metallic layer, and d is the thickness of the dielectric layer (see Fig. 4).

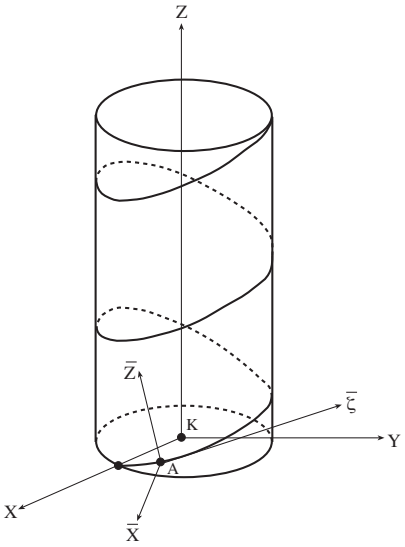

Figure 2. Rotations and translation of the orthogonal system $(\overline{X}, \overline{\zeta}, \overline{Z})$ from point A to the orthogonal system (X, Y, Z) at point K.

Figure 2 shows the rotations and translation of the orthogonal system $(\overline{X}, \overline{\zeta}, \overline{Z})$ from point A to the orthogonal system (X, Y, Z) at point K. In the first rotation, the $\overline{\zeta}$ and $\overline{Z}$ axes rotate around the $\overline{X}$ axis of the orthogonal system $(\overline{X}, \overline{\zeta}, \overline{Z})$ at the point A until the $\overline{Z}$ axis becomes parallel to the Z axis ($\overline{Z} \parallel$ Z), and the $\overline{\zeta}$ axis becomes parallel

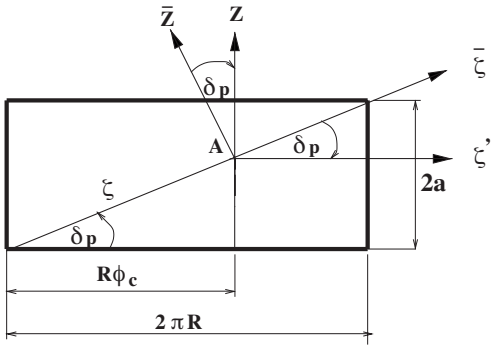

Figure 3. Deployment of the helix.

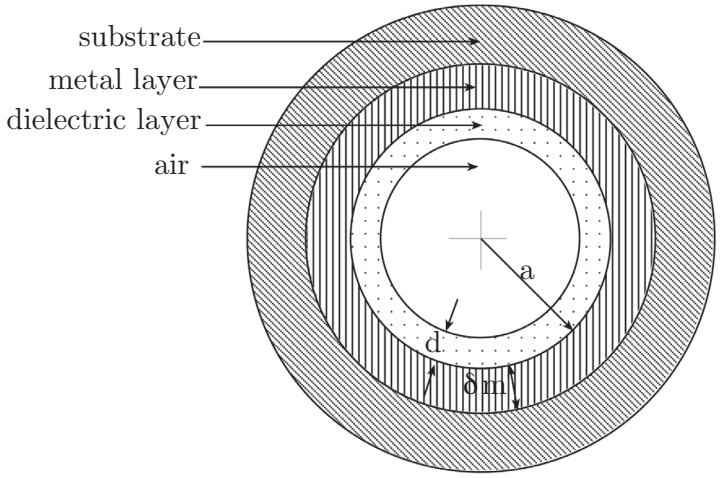

Figure 4. A cross-section of the waveguide (r, θ).

to the X, Y plane ($\overline{\zeta} \parallel (X, Y)$) of the orthogonal system (X, Y, Z) at the point K. In the second rotation, the $\overline{X}$ and $\overline{\zeta}$ axes rotate around the $\overline{Z}$ axis ($\overline{Z} \parallel$ Z) of the orthogonal system ($\overline{X}$, $\overline{\zeta}$, $\overline{Z}$) until $\overline{X} \parallel X$ and $\overline{\zeta} \parallel Y$. After the two above rotations, we have one translation from the orthogonal system $(\overline{X}, \overline{\zeta}, \overline{Z})$ at point A to the orthogonal system (X, Y, Z) at the point K.

Figure 3 shows the deployment of the helix depicted in Fig. 2. The condition for the step's angle δ_p is given according to

$$\tan(\delta_p) \geq \frac{2(a + \delta_m)}{2\pi R}, \tag{2}$$

where the internal diameter is denoted as $2a$, the thickness of the metallic layer is denoted as δ_m, and the radius of the cylinder is denoted as R.

According to Eqs. (1a)–(1c), the helical transformation of the coordinates becomes

$$X = (R + r\sin\theta)\cos(\phi_c) + r\sin(\delta_p)\cos\theta\sin(\phi_c), \tag{3a}$$
$$Y = (R + r\sin\theta)\sin(\phi_c) - r\sin(\delta_p)\cos\theta\cos(\phi_c), \tag{3b}$$
$$Z = r\cos\theta\cos(\delta_p) + \zeta\sin(\delta_p), \tag{3c}$$

where $\phi_c = (\zeta/R)\cos(\delta_p)$, R is the radius of the cylinder, and (r, θ) are the parameters of the cross-section. Note that $\zeta\sin(\delta_p) = R\phi_c\tan(\delta_p)$.

The metric coefficients in the case of the helical waveguide according to Eqs. (3a)–(3c) are:

$$h_r = 1, \tag{4a}$$
$$h_\theta = r, \tag{4b}$$

$$h_\zeta = \sqrt{(1 + \frac{r}{R}\sin\theta)^2\cos^2(\delta_p) + \sin^2(\delta_p)(1 + \frac{r^2}{R^2}\cos^2\theta\cos^2(\delta_p))}$$
$$= \sqrt{1 + \frac{2r}{R}\sin\theta\cos^2(\delta_p) + \frac{r^2}{R^2}\sin^2\theta\cos^2(\delta_p) + \frac{r^2}{R^2}\cos^2\theta\cos^2(\delta_p)\sin^2(\delta_p)}$$
$$\simeq 1 + \frac{r}{R}\sin\theta\cos^2(\delta_p). \tag{4c}$$

Furthermore, the third and the fourth terms in the root of the metric coefficient h_ζ are negligible in comparison to the first and the second terms when $(r/R)^2 \ll 1$. Nonetheless, the metric coefficient h_ζ still depends on δ_p, the step's angle of the helix (Fig. 3). Note that the metric coefficient h_ζ is a function of r and θ, which causes a difficulty in the separation of variables. Thus, the analytical methods are not suitable for the helical or the curved waveguide. In this method, the separation of variables is performed by employing the orthogonal-relations. The cross-section of the helical waveguide in the region $0 \le r \le a + \delta_m$ is shown in Fig. 4, where δ_m is the thickness of the metallic layer, and d is the thickness of the dielectric layer.

For small values of the step's angle δ_p ($\sin(\delta_p) \simeq \tan(\delta_p) \simeq \delta_p, \cos(\delta_p) \simeq 1$), condition (2) becomes $\delta_p \ge 2(a+\delta_m)/(2\pi R)$. For small values of the step's angle, the helical waveguide becomes a toroidal waveguide, where the radius of the curvature of the helix can then be approximately by the radius of the cylinder (R). In this case, the toroidal system (r, θ, ζ) in conjunction with the curved waveguide is

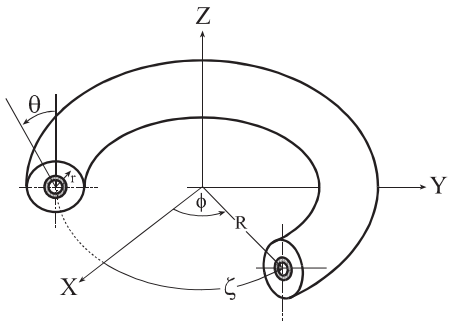

Figure 5. A general scheme of the toroidal system (r, θ, ζ) and the curved waveguide.

shown in Fig. 5, and the transformation of the coordinates (3a)–(3c) is given as a special case of the toroidal transformation of the coordinates, as follows

$$X = (R + r\sin\theta)\cos\left(\frac{\zeta}{R}\right) \ , \quad Y = (R + r\sin\theta)\sin\left(\frac{\zeta}{R}\right) \ , \quad Z = r\cos\theta, \tag{5a, b, c}$$

and the metric coefficients are given by

$$h_r = 1 \ \ , \quad h_\theta = r \ , \quad h_\zeta = 1 + \frac{r}{R}\sin\theta \ \ . \tag{6a, b, c}$$

By using the Serret-Frenet relations for a spatial curve, we can find the curvature (κ) and the torsion (τ) for each spatial curve that is characterized by θ = const and r = const for each pair (r, θ) in the range. This is achieved by using the helical transformation introduced in equations (3a)–(3c). The curvature and the torsion (see Appendix A) are constants for constant values of the radius of the cylinder (R), the step's angle (δ_p) and the parameters (r, θ) of the cross-section. The curvature and the torsion are given by

$$\kappa = \frac{1 + C_t}{R(1 + \tan^2(\delta_p) + C_t)} \quad , \quad \tau = \frac{\tan(\delta_p)}{R(1 + \tan^2(\delta_p) + C_t)}, \tag{7a, b}$$

where

$$C_t = \frac{r^2}{R^2}\sin^2\theta + 2\frac{r}{R}\sin\theta + \frac{r^2}{R^2}\sin^2(\delta_p)\cos^2\theta.$$

The radius of curvature and the radius of torsion are given by $\rho = 1/\ \kappa$, and $\sigma = 1/\ \tau$, respectively. For small values of the step's angle ($\delta_p \ll 1$), the helical waveguide becomes a toroidal waveguide (Fig. 5), where

the radius of the curvature of the helix can then be approximately by the radius of the cylinder ($\rho \simeq R$).

The generalization of the method from a toroidal dielectric waveguide [16] (approximately a plane curve) to a helical waveguide (a space curved waveguide for an arbitrary value of the step's angle of the helix) is presented in the following derivation. The derivation is based on Maxwell's equations for the computation of the EM field and the radiation power density at each point during propagation along a helical waveguide, with a radial dielectric profile. The longitudinal components of the fields are developed into the Fourier-Bessel series. The transverse components of the fields are expressed as a function of the longitudinal components in the Laplace transform domain. Finally, the transverse components of the fields are obtained by using the inverse Laplace transform by the residue method, for an arbitrary value of the step's angle of the helix (δ_p).

3. SOLUTION OF THE WAVE EQUATIONS

The wave equations for the electric and magnetic field components in the inhomogeneous dielectric medium $\epsilon(r)$ are derived in this section for a lossy dielectric media in metallic boundaries of the waveguide. The cross-section of the helical waveguide is shown in Fig. 4 for the application of the hollow waveguide, in the region $0 \leq r \leq a + \delta_m$, where δ_m is the thickness of the metallic layer, and d is the thickness of the dielectric layer.

The derivation is given for the lossless case to simplify the mathematical expressions. In a linear lossy medium, the solution is obtained by replacing the permitivity ϵ by $\epsilon_c = \epsilon - j(\sigma/\omega)$ in the solutions for the lossless case, where ϵ_c is the complex dielectric constant, and σ is the conductivity of the medium. The boundary conditions for a lossy medium are given after the derivation. For most materials, the permeability μ is equal to that of free space ($\mu = \mu_0$). The wave equations for the electric and magnetic field components in the inhomogeneous dielectric medium $\epsilon(r)$ are given by

$$\nabla^2 \boldsymbol{E} + \omega^2 \mu \epsilon \boldsymbol{E} + \nabla \left(\boldsymbol{E} \cdot \frac{\nabla \epsilon}{\epsilon} \right) = 0, \tag{8a}$$

and

$$\nabla^2 \boldsymbol{H} + \omega^2 \mu \epsilon \boldsymbol{H} + \frac{\nabla \epsilon}{\epsilon} \times (\nabla \times \boldsymbol{H}) = 0, \tag{8b}$$

respectively. The transverse dielectric profile ($\epsilon(r)$) is defined as $\epsilon_0(1 + g(r))$, where ϵ_0 represents the vacuum dielectric constant, and

$g(r)$ is its profile function in the waveguide. The normalized transverse derivative of the dielectric profile (g_r) is defined as $(1/\epsilon(r))(\partial\epsilon(r)/\partial r)$.

From the transformation of Eqs. (3a)–(3c) we can derive the Laplacian of the vector $\boldsymbol{E}$ (i.e., $\nabla^2\boldsymbol{E}$), and obtain the wave equations for the electric and magnetic fields in the inhomogeneous dielectric medium. It is necessary to find the values of $\nabla\cdot\boldsymbol{E}$, $\nabla(\nabla\cdot\boldsymbol{E})$, $\nabla\times\boldsymbol{E}$, and $\nabla\times(\nabla\times\boldsymbol{E})$ in order to obtain the value of $\nabla^2\boldsymbol{E}$, where $\nabla^2\boldsymbol{E}=\nabla(\nabla\cdot\boldsymbol{E})-\nabla\times(\nabla\times\boldsymbol{E})$. All these values are dependent on the metric coefficients (4a)–(4c).

The ζ component of $\nabla^2\boldsymbol{E}$ is given by

$$(\nabla^2\boldsymbol{E})_\zeta=\nabla^2E_\zeta+\frac{2}{Rh_\zeta^2}\left[\sin\theta\frac{\partial}{\partial\zeta}E_r+\cos\theta\frac{\partial}{\partial\zeta}E_\theta\right]-\frac{1}{R^2h_\zeta^2}E_\zeta, \quad (9)$$

where

$$\begin{aligned}\nabla^2E_\zeta \;=\; & \frac{\partial^2}{\partial r^2}E_\zeta+\frac{1}{r^2}\frac{\partial^2}{\partial\theta^2}E_\zeta+\frac{1}{r}\frac{\partial}{\partial r}E_\zeta \\ & +\frac{1}{h_\zeta}\left[\frac{\sin\theta}{R}\frac{\partial}{\partial r}E_\zeta+\frac{\cos\theta}{rR}\frac{\partial}{\partial\theta}E_\zeta+\frac{1}{h_\zeta}\frac{\partial^2}{\partial\zeta^2}E_\zeta\right], \quad (10)\end{aligned}$$

and in the case of $h_\zeta=1+(r/R)\sin\theta\cos^2(\delta_p)$.

The longitudinal components of the wave equations (8a) and (8b) are obtained by deriving the following terms

$$\left[\nabla(\boldsymbol{E}\cdot\frac{\nabla\epsilon}{\epsilon})\right]_\zeta=\frac{1}{h_\zeta}\frac{\partial}{\partial\zeta}\left[E_rg_r\right], \quad (11)$$

and

$$\left[\frac{\nabla\epsilon}{\epsilon}\times(\nabla\times\boldsymbol{H})\right]_\zeta=j\omega\epsilon\left[\frac{\nabla\epsilon}{\epsilon}\times\boldsymbol{E}\right]_\zeta=j\omega\epsilon g_rE_\theta. \quad (12)$$

The longitudinal components of the wave equations (8a) and (8b) are then written in the form

$$\left(\nabla^2\boldsymbol{E}\right)_\zeta+k^2E_\zeta+\frac{1}{h_\zeta}\frac{\partial}{\partial\zeta}\left(E_rg_r\right)\;=\;0, \quad (13)$$

$$\left(\nabla^2\boldsymbol{H}\right)_\zeta+k^2H_\zeta+j\omega\epsilon g_rE_\theta\;=\;0, \quad (14)$$

where $(\nabla^2\mathbf{E})_\zeta$, for instance, is given in eq. (9). The *local* wave number parameter is $k=\omega\sqrt{\mu\epsilon(r)}=k_0\sqrt{1+g(r)}$, where the free-space wave number is $k_0=\omega\sqrt{\mu_0\epsilon_0}$.

The transverse Laplacian operator is defined as

$$\nabla_{\perp}^2 \equiv \nabla^2 - \frac{1}{h_\zeta^2}\frac{\partial^2}{\partial \zeta^2}. \tag{15}$$

The Laplace transform

$$\tilde{a}(s) = \mathcal{L}\{a(\zeta)\} = \int_{\zeta=0}^{\infty} a(\zeta) e^{-s\zeta} d\zeta \tag{16}$$

is applied on the ζ-dimension, where $a(\zeta)$ represents any ζ-dependent variables, where $\zeta = (R\phi_c)/\cos(\delta_p)$.

The next steps are given in detail in Ref. [16], as a part of our derivation. Let us repeat these steps, in brief.

1). By substituting Eq. (9) into Eq. (13) and by using the Laplace transform (16), the longitudinal components of the wave equations (Eqs. (13)–(14)) are described in the Laplace transform domain, as *coupled* wave equations.

2). The transverse fields are obtained directly from Maxwell's equations, and by using the Laplace transform (16), and are given by

$$\begin{aligned}\tilde{E}_r(s) = \frac{1}{s^2+k^2h_\zeta^2}\Bigg\{ &-\frac{j\omega\mu_0}{r}\left[\frac{r}{R}\cos\theta\cos^2(\delta_p)\tilde{H}_\zeta + h_\zeta\frac{\partial}{\partial\theta}\tilde{H}_\zeta\right]h_\zeta \\ &+s\left[\frac{\sin\theta}{R}\cos^2(\delta_p)\tilde{E}_\zeta + h_\zeta\frac{\partial}{\partial r}\tilde{E}_\zeta\right] + sE_{r_0} - j\omega\mu_0 H_{\theta_0}h_\zeta\Bigg\},\end{aligned} \tag{17a}$$

$$\begin{aligned}\tilde{E}_\theta(s) = \frac{1}{s^2+k^2h_\zeta^2}\Bigg\{ &\frac{s}{r}\left[\frac{r}{R}\cos\theta\cos^2(\delta_p)\tilde{E}_\zeta + h_\zeta\frac{\partial}{\partial\theta}\tilde{E}_\zeta\right] \\ &+j\omega\mu_0 h_\zeta\left[\frac{\sin\theta}{R}\cos^2(\delta_p)\tilde{H}_\zeta + h_\zeta\frac{\partial}{\partial r}\tilde{H}_\zeta\right] + sE_{\theta_0} + j\omega\mu_0 H_{r_0}h_\zeta\Bigg\},\end{aligned} \tag{17b}$$

$$\begin{aligned}\tilde{H}_r(s) = \frac{1}{s^2+k^2h_\zeta^2}\Bigg\{ &\frac{j\omega\epsilon}{r}\left[\frac{r}{R}\cos\theta\cos^2(\delta_p)\tilde{E}_\zeta + h_\zeta\frac{\partial}{\partial\theta}\tilde{E}_\zeta\right]h_\zeta \\ &+s\left[\frac{\sin\theta}{R}\cos^2(\delta_p)\tilde{H}_\zeta + h_\zeta\frac{\partial}{\partial r}\tilde{H}_\zeta\right] + sH_{r_0} + j\omega\epsilon E_{\theta_0}h_\zeta\Bigg\},\end{aligned} \tag{17c}$$

$$\begin{aligned}\tilde{H}_\theta(s) = \frac{1}{s^2+k^2h_\zeta^2}\Bigg\{ &\frac{s}{r}\left[\frac{r}{R}\cos\theta\cos^2(\delta_p)\tilde{H}_\zeta + h_\zeta\frac{\partial}{\partial\theta}\tilde{H}_\zeta\right] \\ &-j\omega\epsilon h_\zeta\left[\frac{\sin\theta}{R}\cos^2(\delta_p)\tilde{E}_\zeta + h_\zeta\frac{\partial}{\partial r}\tilde{E}_\zeta\right] + sH_{\theta_0} - j\omega\epsilon E_{r_0}h_\zeta\Bigg\}.\end{aligned} \tag{17d}$$

Note that the transverse fields are dependent only on the longitudinal components of the fields and as function of the step's angle (δ_p) of the helix.

3). The transverse fields are substituted into the *coupled* wave equations.

4). The longitudinal components of the fields are developed into Fourier-Bessel series, in order to satisfy the metallic boundary conditions of the circular cross-section. The condition is that we have only ideal boundary conditions for $r = a$. Thus, the electric and magnetic fields will be zero in the metal.

5). Two sets of equations are obtained by substitution the longitudinal components of the fields into the wave equations. The first set of the equations is multiplied by $\cos(n\theta)J_n(P_{nm}r/a)$, and after that by $\sin(n\theta)J_n(P_{nm}r/a)$, for $n \neq 0$. Similarly, the second set of the equations is multiplied by $\cos(n\theta)J_n(P'_{nm}r/a)$, and after that by $\sin(n\theta)J_n(P'_{nm}r/a)$, for $n \neq 0$.

6). In order to find an algebraic system of four equations with four unknowns, it is necessary to integrate over the area (r, θ), where $r = [0, a]$, and $\theta = [0, 2\pi]$, by using the orthogonal-relations of the trigonometric functions.

7). The propagation constants β_{nm} and β'_{nm} of the TM and TE modes of the hollow waveguide [17] are given, respectively, by $\beta_{nm} = \sqrt{k_o^2 - (P_{nm}/a)^2}$ and $\beta'_{nm} = \sqrt{k_o^2 - (P'_{nm}/a)^2}$, where the transverse Laplacian operator $(\nabla_\perp^2)$ is given by $-(P_{nm}/a)^2$ and $-(P'_{nm}/a)^2$ for the TM and TE modes of the hollow waveguide, respectively.

The separation of variables is obtained by using the preceding orthogonal-relations. Thus the algebraic equations ($n \neq 0$) are given by

$$\alpha_n{}^{(1)}A_n + \beta_n{}^{(1)}D_n = \frac{1}{\pi}(\widehat{BC1})_n, \tag{18a}$$

$$\alpha_n{}^{(2)}B_n + \beta_n{}^{(2)}C_n = \frac{1}{\pi}(\widehat{BC2})_n, \tag{18b}$$

$$\beta_n{}^{(3)}B_n + \alpha_n{}^{(3)}C_n = \frac{1}{\pi}(\widehat{BC3})_n, \tag{18c}$$

$$\beta_n{}^{(4)}A_n + \alpha_n{}^{(4)}D_n = \frac{1}{\pi}(\widehat{BC4})_n. \tag{18d}$$

Further we assume $n' = n = 1$. The elements ($\alpha_n{}^{(1)}$, $\beta_n{}^{(1)}$, etc.), on the left side of (18a) for $n = 1$ are given for an arbitrary value of the

step's angle (δ_p) by:

$$
\begin{aligned}
{\alpha_1}^{(1)mm'} = {} & \pi\left(s^2+\beta_{1m'}^2\right)\left[\left(s^2+{k_0}^2\right)G_{00}^{(1)mm'}+{k_0}^2G_{01}^{(1)mm'}\right] \\
& +\pi\frac{1}{R^4}{k_0}^2s^2\left(\frac{1}{4}\cos^4(\delta_p)G_{02}^{(1)mm'}+\frac{1}{2}\cos^4(\delta_p)G_{03}^{(1)mm'}\right) \\
& +\pi{k_0}^2\Bigg\{s^2G_{01}^{(1)mm'}+G_{05}^{(1)mm'}+\frac{1}{R^2}\left(G_{00}^{(1)mm'}+G_{01}^{(1)mm'}\right) \\
& \quad +\frac{3}{2R^2}\beta_{1m'}^2\cos^4(\delta_p)\left(G_{02}^{(1)mm'}+G_{03}^{(1)mm'}\right) \\
& \quad +\frac{1}{4R^4}\cos^4(\delta_p)\left(G_{02}^{(1)mm'}+G_{03}^{(1)mm'}\right) \\
& \quad +\frac{1}{8R^4}\cos^8(\delta_p)\left(G_{06}^{(1)mm'}+G_{07}^{(1)mm'}\right)\Bigg\} \\
& +\pi s^2\Bigg[G_{08}^{(1)mm'}+\frac{1}{2R^2}\cos^2(\delta_p)G_{00}^{(1)mm'} \\
& \quad +\frac{1}{4R^2}\left(\cos^4(\delta_p)\beta_{1m'}^2G_{02}^{(1)mm'}+\cos^2(\delta_p)G_{09}^{(1)mm'}\right) \\
& \quad +\frac{1}{2R^2}\frac{P_{1m'}}{a}\cos^2(\delta_p)\left(G_{10}^{(1)mm'}+\frac{1}{2}\cos^2(\delta_p)G_{11}^{(1)mm'}\right)\Bigg] \\
& +\pi{k_0}^4\cos^4(\delta_p)\Bigg[\frac{3}{2R^2}\left(G_{03}^{(1)mm'}+G_{04}^{(1)mm'}\right) \\
& \quad +\frac{1}{8R^4}\cos^8(\delta_p)\left(G_{07}^{(1)mm'}+G_{12}^{(1)mm'}\right)\Bigg], \qquad (19a)
\end{aligned}
$$

$$
\begin{aligned}
{\beta_1}^{(1)mm'} = {} & -j\omega\mu_0\pi s\Bigg\{G_{13}^{(1)mm'}+\left(\frac{1}{2}\cos^2(\delta_p)+\frac{3}{4}\cos^4(\delta_p)\right)\frac{1}{R^2}G_{14}^{(1)mm'} \\
& +\left(\frac{1}{2}+\cos^2(\delta_p)\right)\frac{1}{R^2}G_{15}^{(1)mm'} \\
& -\frac{1}{2R^2}G_{00}^{(1)mm'}-\cos^2(\delta_p)\frac{1}{R^2}\frac{P'_{1m'}}{a}G_{16}^{(1)mm'}\Bigg\}, \qquad (19b)
\end{aligned}
$$

where the elements of the matrices ($G_{00}^{(1)mm'}$, etc.) are given in Appendix B. Similarly, the rest of the elements on the left side in

Eqs. (18a)–(18d) are obtained. We establish an algebraic system of four equations with four unknowns. All the elements of the matrices in the Laplace transform domain are dependent on the step's angle of the helix (δ_p), the Bessel functions; the dielectric profile $g(r)$; the transverse derivative $g_r(r)$; and (r, θ).

The elements of the boundary conditions (e.g., $(\widehat{BC2})_1$) at $\zeta = 0^+$ on the right side in (18b) are dependent on the step's angle δ_p as follows:

$$(\widehat{BC2})_1 = \int_0^{2\pi} \int_0^a (BC2) \sin\theta J_1(P_{1m} r/a) r dr d\theta,$$

where

$$\begin{aligned}(BC2) \;=\; & \left[\left(s^2 + k^2 h_\zeta^2\right)\left(sE_{\zeta_0} + E'_{\zeta_0}\right)\right] + j\omega\mu_0 H_{\theta_0} s g_r h_\zeta^2 \\ & + \frac{2}{R} h_\zeta \sin\theta \left(j\omega\mu_0 H_{\theta_0} s + k^2 E_{r_0} h_\zeta\right) \\ & + \frac{2}{R} h_\zeta \cos\theta \left(-j\omega\mu_0 H_{r_0} s + k^2 E_{\theta_0} h_\zeta\right) + k^2 h_\zeta^3 E_{r_0} g_r,\end{aligned}$$

and for $h_\zeta = 1 + \frac{r}{R}\sin\theta\cos^2(\delta_p)$.

The boundary conditions at $\zeta = 0^+$ for TEM_{00} mode in excitation become to:

$$\begin{aligned}(\widehat{BC2})_1 \;=\; & 2\pi\left\{\int_0^a Q(r)(k(r) + js) J_{1m}(P_{1m} r/a) r dr\right\}\delta_{1n} \\ & + \frac{4js\pi}{R^2}\cos^2(\delta_p)\left\{\int_0^a Q(r) k(r) J_{1m}(P_{1m} r/a) r^2 dr\right\}\delta_{1n} \\ & + \frac{9\pi}{2R^2}\cos^4(\delta_p)\left\{\int_0^a Q(r) k^2(r) J_{1m}(P_{1m} r/a) r^3 dr\right\}\delta_{1n} \\ & + \frac{3js\pi}{2R^2}\cos^4(\delta_p)\left\{\int_0^a Q(r) k(r) J_{1m}(P_{1m} r/a) r^3 dr\right\}\delta_{1n} \\ & + \frac{8\pi}{R^2}\cos^2(\delta_p)\left\{\int_0^a Q(r) k^2(r) J_{1m}(P_{1m} r/a) r^2 dr\right\}\delta_{1n} \quad (20)\end{aligned}$$

where :

$$Q(r) = \frac{E_0}{n_c(r) + 1} g_r \exp\left(-(r/w_o)^2\right).$$

Similarly, the remaining elements of the boundary conditions at $\zeta = 0^+$ are obtained. The matrix system of Eqs. (18a)–(18d) is solved to obtain the coefficients (A_1, B_1, etc).

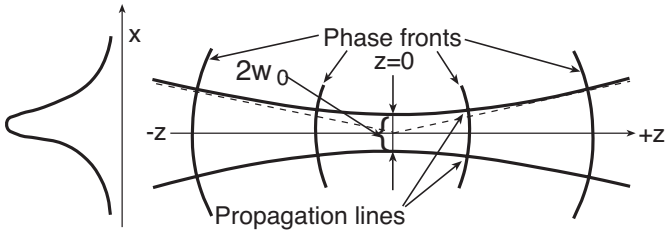

Figure 6. Propagating Gaussian beam.

According to the Gaussian beams [18] the parameter w_0 is the minimum spot-size at the plane $z = 0$ (see Fig. 6), and the electric field at the plane $z = 0$ is given by $E = E_0 \exp[-(r/w_o)^2]$. The modes excited at $\zeta = 0$ in the waveguide by the conventional CO_2 laser IR radiation ($\lambda = 10.6\,\mu$m) are closer to the TEM polarization of the laser radiation. The TEM_{00} mode is the fundamental and most important mode. This means that a cross-section of the beam has a Gaussian intensity distribution. The relation between the electric and magnetic fields [18] is given by $E/H = \sqrt{\mu_0/\epsilon_0} \equiv \eta_0$, where η_0 is the intrinsic wave impedance. Suppose that the electric field is parallel to the y-axis. Thus the components of E_y and H_x are written by the fields $E_y = E_0 \exp[-(r/w_o)^2]$ and $H_x = -(E_0/\eta_0) \exp[-(r/w_o)^2]$.

After a Gaussian beam passes through a lens and before it enters to the waveguide, the waist cross-sectional diameter ($2w_0$) can then be approximately calculated for a parallel incident beam by means of $w_0 = \lambda/(\pi\,\theta) \simeq (f\lambda)/(\pi w)$. This approximation is justified if the parameter w_0 is much larger than the wavelength λ. The parameter of the waist cross-sectional diameter ($2w_0$) is taken into account in our method, instead of the focal length of the lens (f). The initial fields at $\zeta = 0^+$ are formulated by using the Fresnel coefficients of the transmitted fields [19] as follows

$$E^+_{r_0}(r) = T_E(r)(E_0 e^{-(r/w_o)^2} \sin\theta), \tag{21a}$$

$$E^+_{\theta_0}(r) = T_E(r)(E_0 e^{-(r/w_o)^2} \cos\theta), \tag{21b}$$

$$H^+_{r_0}(r) = -T_H(r)((E_0/\eta_0) e^{-(r/w_o)^2} \cos\theta), \tag{21c}$$

$$H^+_{\theta_0}(r) = T_H(r)((E_0/\eta_0) e^{-(r/w_o)^2} \sin\theta), \tag{21d}$$

where $E^+_{\zeta_0} = H^+_{\zeta_0} = 0$, $T_E(r) = 2/[(n(r)+1]$, $T_H(r) = 2n(r)/[(n(r)+1]$,

and $n(r) = [\epsilon_r(r)]^{1/2}$. The index of refraction is denoted by $n(r)$.

The transverse components of the fields are finally expressed in a form of *transfer matrix functions* for an arbitrary value of δ_p as follows:

$$\begin{aligned} E_r(r,\theta,\zeta) = {} & E_{r0}^{+}(r)e^{-jkh_\zeta\zeta} - \frac{j\omega\mu_0}{R}h_\zeta\cos^2\theta\cos^2(\delta_p)\sum_{m'}C_{S1}^{m'}(\zeta)J_1(\psi) \\ & -\frac{j\omega\mu_0}{R}h_\zeta\sin\theta\cos\theta\cos^2(\delta_p)\sum_{m'}D_{S1}^{m'}(\zeta)J_1(\psi) \\ & +\frac{j\omega\mu_0}{r}h_\zeta^2\sin\theta\sum_{m'}C_{S1}^{m'}(\zeta)J_1(\psi) \\ & -\frac{j\omega\mu_0}{r}h_\zeta^2\cos\theta\sum_{m'}D_{S1}^{m'}(\zeta)J_1(\psi) \\ & +\frac{1}{R}\sin\theta\cos\theta\cos^2(\delta_p)\sum_{m'}A_{S2}^{m'}(\zeta)J_1(\xi) \\ & +\frac{1}{R}\sin^2\theta\cos^2(\delta_p)\sum_{m'}B_{S2}^{m'}(\zeta)J_1(\xi) \\ & +h_\zeta\cos\theta\sum_{m'}A_{S2}^{m'}(\zeta)\frac{dJ_1}{dr}(\xi) + h_\zeta\sin\theta\sum_{m'}B_{S2}^{m'}(\zeta)\frac{dJ_1}{dr}(\xi), \end{aligned} \tag{22}$$

where $h_\zeta = 1+(r/R)\sin\theta\cos^2(\delta_p)$, R is the radius of the cylinder, δ_p is the step's angle, $\psi = [P'_{1m'}(r/a)]$ and $\xi = [P_{1m'}(r/a)]$. The coefficients are given in the above equation, for instance

$$A_{S1}^{m'}(\zeta) = \mathcal{L}^{-1}\left\{\frac{A_{1m'}(s)}{s^2+k^2(r)h_\zeta^2}\right\}, \tag{23a}$$

$$A_{S2}^{m'}(\zeta) = \mathcal{L}^{-1}\left\{\frac{sA_{1m'}(s)}{s^2+k^2(r)h_\zeta^2}\right\}, \tag{23b}$$

where

$$m' = 1,\ldots N, \qquad 3 \le N \le 50. \tag{23c}$$

Similarly, the other transverse components of the output fields are obtained (see Appendix C). The first fifty roots (zeros) of the equations $J_1(x) = 0$ and $dJ_1(x)/dx = 0$ may be found in tables [20, 21].

The inverse Laplace transform is performed in this study by a direct numerical integration in the Laplace transform domain by the

residue method, as follows

$$f(\zeta) = \mathcal{L}^{-1}[\tilde{f}(s)] = \frac{1}{2\pi j}\int_{\sigma-j_\infty}^{\sigma+j_\infty} \tilde{f}(s)e^{s\zeta}ds = \sum_n Res[e^{s\zeta}\tilde{f}(s); S_n]. \tag{24}$$

By using the inverse Laplace transform (24) we can compute the output transverse components in the real plane and the output power density at each point at $\zeta = (R\phi_c)/\cos(\delta_p)$. The integration path in the right side of the Laplace transform domain includes all the singularities according to Eq. (24). All the points S_n are the poles of $\tilde{f}(s)$ and $Res[e^{s\zeta}\tilde{f}(s); S_n]$ represent the residue of the function in a specific pole. According to the residue method, two dominant poles for the helical waveguide are given by

$$s = \pm j\ k(r)h_\zeta = \pm j\ k(r)\left(1 + \frac{r}{R}\sin\theta\cos^2(\delta_p)\right).$$

Finally, knowing all the transverse components, the ζ component of the average-power density Poynting vector is given by

$$S_{av} = \frac{1}{2}Re\left\{E_r H_\theta{}^* - E_\theta H_r{}^*\right\}, \tag{25}$$

where the asterisk indicates the complex conjugate.

The total average-power transmitted along the guide in the ζ direction can now be obtained by the integral of Eq. (25) over the waveguide cross section. Thus, the output power transmission is given by

$$T = \frac{1}{2}\int_0^{2\pi}\int_0^a Re\left\{E_r H_\theta{}^* - E_\theta H_r{}^*\right\} r dr d\theta\ . \tag{26}$$

Lossy medium case

In a linear lossy medium, the solution is obtained by replacing the permitivity ϵ by $\epsilon_c = \epsilon - j(\sigma/\omega)$ in the preceding mathematical expressions, where ϵ_c is the complex dielectric constant and σ is the conductivity of the medium. The coefficients are obtained directly from the algebraic equations (18a)–(18d) and are expressed as functions in the Laplace transform domain. To satisfy the metallic boundary conditions of a circular cross-section we find the new roots $P_{1m}^{(new)}$ and $P_{1m}^{'(new)}$ of the equations $J_1(z) = 0$ and $dJ_1(z)/dz = 0$, respectively, where z is complex. Thus, from the requirement that the coefficients vanish, the new roots $P_{1m}^{(new)}$ and $P_{1m}^{'(new)}$ are calculated by developing

into the Taylor series, in the first order at $1/\sigma$. The new roots in the case of a lossy medium are complex. The complex Bessel functions are computed by using NAG subroutine [22]. The explanation is given in detail in Ref. [16].

It should be noticed that a theoretical method [23] has been developed also for a curved waveguide with a rectangular cross section. Several examples computed on a Unix system are presented in the next sections, in order to demonstrate the results of this proposed method for a helical waveguide (a space curved waveguide for an arbitrary value of the step's angle of the helix) in the case of a hollow waveguide. We suppose that the transmitted fields of the initial fields (TEM_{00} mode in excitation) are formulated by using the Fresnel coefficients (21a)–(21d).

4. NUMERICAL RESULTS

The next examples represent the case of the hollow waveguide with a metallic layer (Ag) coated by a thin dielectric layer (AgI). For silver having a conductivity of $6.14 \times 10^7 (\text{ohm} \cdot \text{m})^{-1}$ and the skin depth at 10.6 μm is 1.207×10^{-8} m. Three test-cases are demonstrated for small values of the step's angle (δ_p). In these cases, the condition (2) becomes $\delta_p \geq 2(a + \delta_m)/(2\pi R)$. Note that for small values of the step's angle, the helical waveguide becomes approximately a toroidal waveguide (see Fig. 5), where the radius of the curvature of the helix (ρ) can then be approximately by the radius of the cylinder (R).

The first test-case is demonstrated for the straight waveguide ($R \to \infty$). The results of the output transverse components of the fields and the output power density ($|S_{av}|$) (e.g., Fig. 7(a)) show the same behavior of the solutions as shown in the results of Ref. [16] for the TEM_{00} mode in excitation. The result of the output power density (Fig. 7(a)) is compared also to the result of published experimental data [24] (see also in Fig. 7(b)). This comparison shows good agreement (a Gaussian shape) as expected, except for the secondary small propagation mode. In this example, the length of the straight waveguide is 1 m, the diameter (2a) of the waveguide is 2 mm, the thickness of the dielectric layer [$d_{(AgI)}$] is 0.75 μm, and the minimum spot-size (w_0) is 0.3 mm. The refractive indices of the air, dielectric layer (AgI) and metallic layer (Ag) are $n_{(0)} = 1$, $n_{(AgI)} = 2.2$, and $n_{(Ag)} = 13.5 - j75.3$, respectively. The value of the refractive index of the material at a wavelength of $\lambda = 10.6\,\mu$m is taken from the table compiled by Miyagi et al. in Ref. [5].

The second test-case is demonstrated in Fig. 8(a) for the toroidal dielectric waveguide. Fig. 8(b) shows the experimental result that

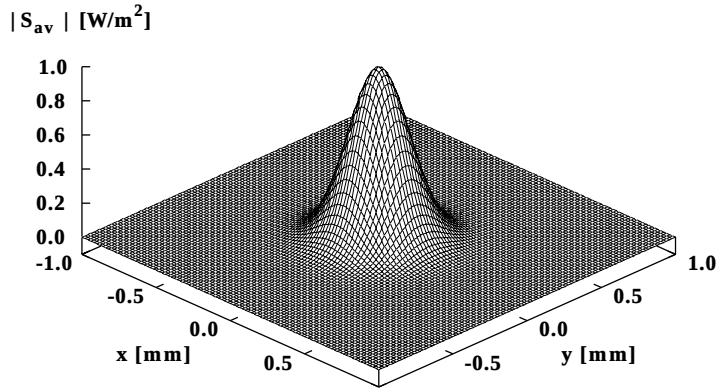

(a)

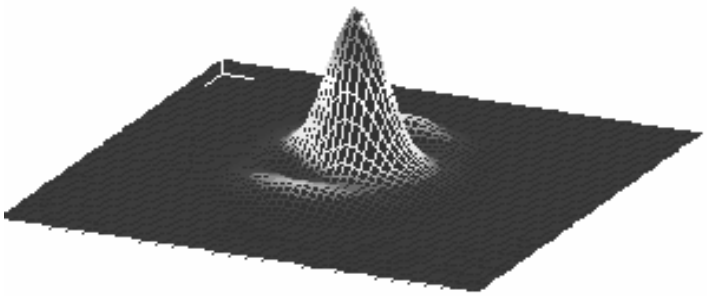

(b)

Figure 7. The output power density ($a = 1\,\text{mm}$, $d_{(AgI)} = 0.75\,\mu\text{m}$, $\lambda = 10.6\,\mu\text{m}$, $w_0 = 0.3\,\text{mm}$, $n_{(0)} = 1$, $n_{(AgI)} = 2.2$, $n_{(Ag)} = 13.5 - j75.34$, and the length of the straight waveguide is 1 m), for $R \to \infty$: (a) theoretical result; (b) experimental result.

was received in the laboratory of Croitoru at Tel-Aviv University. This experimental result was obtained from the measurements of the transmitted CO_2 laser radiation ($\lambda = 10.6\,\mu\text{m}$) propagation through a hollow tube covered on the bore wall with silver and silver-iodide layers (Fig. 4), where the initial diameter (ID) is 1 mm (namely, small bore size).

The output modal profile is greatly affected by the bending, and the theoretical and experimental results (Figs. 8(a)–8(b)) show that in addition to the main propagation mode, several other secondary modes and asymmetric output shape appear. The amplitude of the output

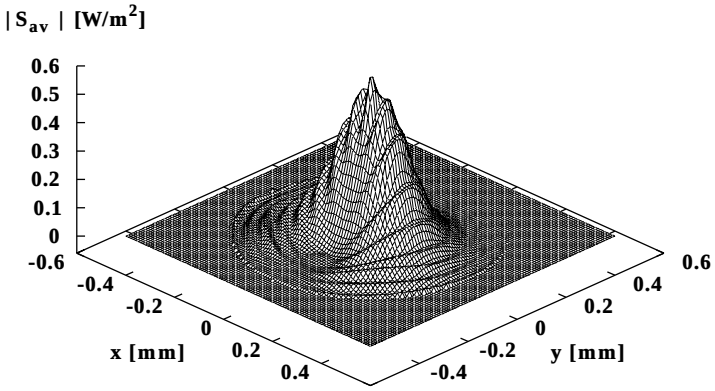

(a)

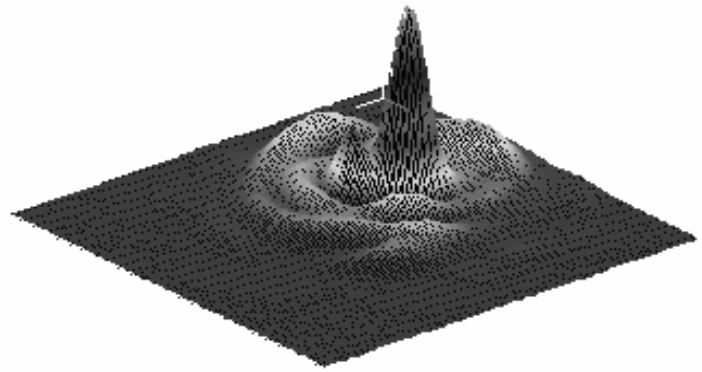

(b)

Figure 8. Solution of the output power density ($a = 0.5\,\text{mm}$, $d_{(AgI)} = 0.75\,\mu\text{m}$, $\lambda = 10.6\,\mu\text{m}$, $w_0 = 0.2\,\text{mm}$, $n_{(0)} = 1$, $n_{(AgI)} = 2.2$, $n_{(Ag)} = 13.5 - j75.3$, $R = 0.7\,\text{m}$, $\phi = \pi/2$, and $\zeta = 1\,\text{m}$): (a) theoretical result; (b) experimental result.

power density ($|S_{av}|$) is small for bending radii (R), and the shape is far from a Gaussian shape. This result agrees with the experimental results, but not for all propagation modes. The experimental result (Fig. 8(b)) is influenced by the bending and additional parameters (e.g., the roughnes of the internal wall of the waveguide) which are not taken into account theoretically. In this example, $a = 0.5\,\text{mm}$, $R = 0.7\,\text{m}$, $\phi = \pi/2$, and $\zeta = 1\,\text{m}$. The thickness of the dielectric layer $[d_{(AgI)}]$ is $0.75\,\mu\text{m}$ (Fig. 4), and the minimum spot size (w_0) is $0.2\,\text{mm}$. The values of the refractive indices of the air, dielectric layer (AgI) and

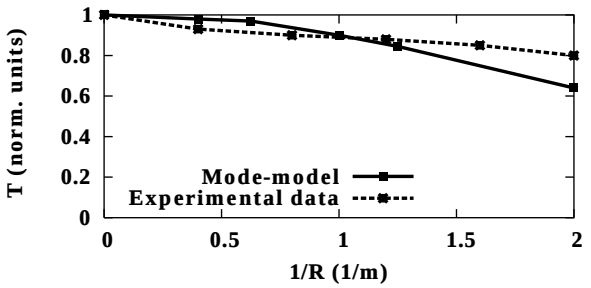

Figure 9. The theoretical mode-model's result and the experimental result [11] where the hollow metallic waveguide (Ag) is covered inside the walls with a AgI film. The output power transmission as a function of $1/R$ for $\delta_p = 0$, where $\zeta = 0.55\,\mathrm{m}$, where $a = 1.2\,\mathrm{mm}$, $d_{(AgI)} = 0.75\,\mu\mathrm{m}$, $w_0 = 0.1\,\mathrm{mm}$, $\lambda = 10.6\,\mu\mathrm{m}$, $n_{(0)} = 1$, $n_{(AgI)} = 2.2$, and $n_{(Ag)} = 10$.

metallic layer (Ag) are $n_{(0)} = 1$, $n_{(AgI)} = 2.2$, and $n_{(Ag)} = 13.5 - j75.3$, respectively. In both theoretical and experimental results (Figs. 8(a)–8(b)) the shapes of the output power density for the curved waveguide are not symmetric.

The third test-case is demonstrated in Fig. 9 for the toroidal dielectric waveguide. The theoretical mode-model's result and the experimental result [11] are demonstrated in normalized units where the length of the curved waveguide (ζ) is 0.55 m, the diameter (2a) of the waveguide is 2.4 mm, and the minimum spot size (w_0) is 0.1 mm.

This comparison (Fig. 9) between the theoretical mode-model and the experimental data [11] indicates a good agreement. For all the examples, our theoretical mode-model takes into account only the dielectric losses and the bending losses, in conjunction with the problem of the propagation through a curved waveguide. The experimental result [11] takes into account additional parameters (e.g., the roughnes of the internal wall of the waveguide) which are not taken into account theoretically. In spite of the differences, the comparison shows a good agreement. For small values of the bending ($1/R$) in the case of small step's angle, the output power transmission is large and decreases with increasing the bending.

Figure 10 demonstrates the influence of the step's angle (δ_p) and the radius of the cylinder (R) on the radius of curvature of the helix (ρ) along the ζ-axis of the helix. Three results are demonstrated for three values of δ_p ($\delta_p = 0, 0.4, 0.8$). For an arbitrary value of radius of cylinder (R), the radius of curvature of the helix (ρ) is large for large values of the step's angle and decreases with decreasing the value

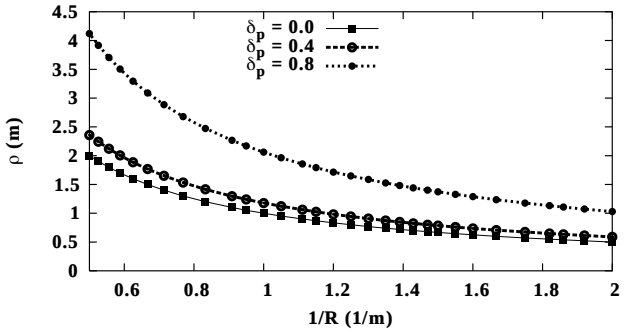

Figure 10. The radius of curvature of the helix (ρ) along the ζ-axis of the helix as a function of $1/R$, where R is the radius of the cylinder. Three results are demonstrated for three values of δ_p ($\delta_p = 0, 0.4, 0.8$).

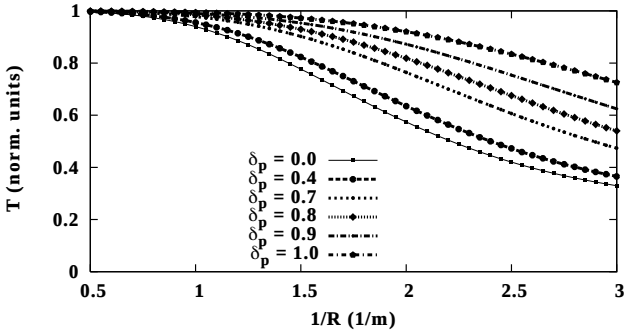

Figure 11. The results of the output power transmission of the helical waveguide as a function of $1/R$, where R is the radius of the cylinder. Six results are demonstrated for six values of δ_p ($\delta_p = 0, 0.4, 0.7, 0.8, 0.9, 1$), where $\zeta = 4\,\mathrm{m}$, $a = 1\,\mathrm{mm}$, $w_0 = 0.06\,\mathrm{mm}$, $n_d = 2.2$, and $n_{(Ag)} = 13.5 - j75.3$.

of δ_p. On the other hand, for an arbitrary value of the step's angle, the radius of curvature of the helix (ρ) is large for large values of the radius of the cylinder (R), and decreases with decreasing the value of the radius of the cylinder.

The main contribution of this paper is demonstrated in Fig. 11, in order to understand the influence of the step's angle (δ_p) and the radius of the cylinder (R) on the output power transmission, defined in Eq. (26). Six results are demonstrated for six values of δ_p ($\delta_p = 0, 0.4, 0.7, 0.8, 0.9, 1.0$), where $\zeta = 4\,\mathrm{m}$, $a = 1\,\mathrm{mm}$, $w_0 = 0.06\,\mathrm{mm}$,

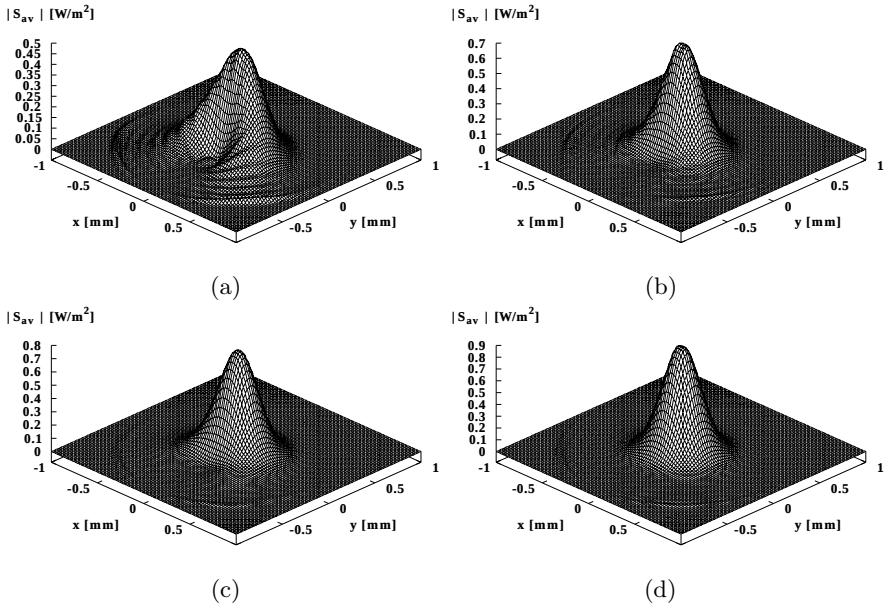

Figure 12. The results of the output power density as functions of the step's angle (δ_p) and the radius of the cylinder (R), where $\zeta = 1\,\mathrm{m}$, $a = 1\,\mathrm{mm}$, $w_0 = 0.3\,\mathrm{mm}$, $n_d = 2.2$, and $n_{(Ag)} = 13.5 - j75.3$: (a). $\delta_p = 0.4$, and $R = 0.7\,\mathrm{m}$; (b). $\delta_p = 0.8$, and $R = 0.7\,\mathrm{m}$; (c). $\delta_p = 0.4$, and $R = 1\,\mathrm{m}$; (d). $\delta_p = 0.8$, and $R = 1\,\mathrm{m}$.

$n_d = 2.2$ and $n_{(Ag)} = 13.5 - j75.3$. For an arbitrary value of R, the output power transmission is large for large values of δ_p and decreases with decreasing the value of δ_p. On the other hand, for an arbitrary value of δ_p, the output power transmission is large for large values of R and decreases with decreasing the value of R. Note that for small values of the step's angle, the radius of curvature of the helix (ρ) can be approximated by the radius of the cylinder (R). In this case, the output power transmission is large for small values of the bending ($1/R$), and decreases with increasing the bending. Thus, this model can be a useful tool to find the parameters (δ_p and R) which will give us the improved results (output power transmission) of a hollow waveguide in the cases of space curved waveguides.

Figures 12(a)–(d) show the results of the output power density as functions of the step's angle (e.g., $\delta_p = 0.4, 0.8$) and the radius of the cylinder (e.g., $R = 0.7\,\mathrm{m}$, $1\,\mathrm{m}$). For these results $\zeta = 1\,\mathrm{m}$, where $a = 1\,\mathrm{mm}$, $w_0 = 0.3\,\mathrm{mm}$, $n_d = 2.2$, and $n_{(Ag)} = 13.5 - j75.3$. For $\delta_p = 0.4$, the amplitude of the output power density is small

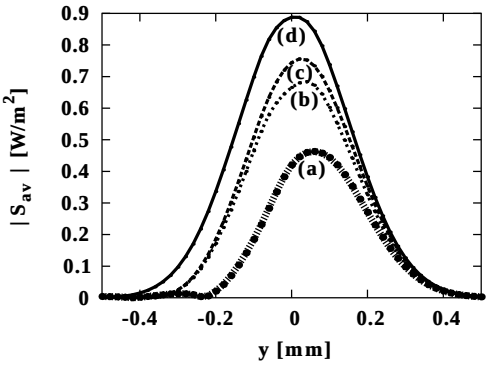

Figure 13. The output amplitude, the width of the Gaussian shape, and the shift of the central peak in the same cross section of Figs. 12(a)–(d) where $x = 0$ and $y = [-0.5\,\text{mm}, +0.5\,\text{mm}]$. Four examples are demonstrated for: (a) $\delta_p = 0.4$, and $R = 0.7\,\text{m}$; (b) $\delta_p = 0.8$, and $R = 0.7\,\text{m}$; (c) $\delta_p = 0.4$, and $R = 1\,\text{m}$; (d) $\delta_p = 0.8$, and $R = 1\,\text{m}$. The output modal profile is greatly affected for small values of δ_p and R, as shown in case (a).

(e.g., ($|S_{av}| = 0.5\,\text{W/m}^2$) as the radius of the cylinder is small (e.g., $R = 0.7\,\text{m}$), and the output shape (Fig. 12(a)) is far from a Gaussian shape (Fig. 12(d)). By increasing only the step's angle from $\delta_p = 0.4$ to $\delta_p = 0.8$ where $R = 0.7\,\text{m}$, the amplitude of the output power density is greater and also the output shape is changed (Fig. 12(b)). By increasing only the radius of the cylinder from 0.7 m to 1 m where $\delta_p = 0.4$, the result of the output power density ($|S_{av}|$) shows a Gaussian shape, and the amplitude of the output power density is changed from $0.5\,\text{W/m}^2$ (Fig. 12(a)) to $0.8\,\text{W/m}^2$ (Fig. 12(c)). Now, by increasing the step's angle from $\delta_p = 0.4$ to $\delta_p = 0.8$ and also by increasing the radius of the cylinder from 0.7 m to 1 m, the result becomes a Gaussian shape (Fig. 12(d)), where the amplitude is changed from $0.5\,\text{W/m}^2$ (Fig. 12(a)) to $0.9\,\text{W/m}^2$. Fig. 12(a) shows that in addition to the main propagation mode, several other secondary modes appear, where $\delta_p = 0.4$ and $R = 0.7\,\text{m}$.

Figures 13(a)–(d) show the output amplitude, the width of the Gaussian shape, and the shift of the central peak in the same cross section of Figs. 12(a)–(d), where $x = 0$ and $y = [-0.5\,\text{mm}, +0.5\,\text{mm}]$. These results represent the output power density as functions of the step's angle (δ_p) and the radius of the cylinder (R), for the same parameters of Figs. 12(a)–(d). By increasing only the step's angle from $\delta_p = 0.4$ to $\delta_p = 0.8$ where $R = 0.7\,\text{m}$, the amplitude and the

width of the Gaussian shape are greater (Fig. 13(b)). In addition, the output shape is improved from asymmetric shape (Fig. 13(a)) to the symmetric shape (Fig. 13(b)). The peak of the output shape (Fig. 13(b)) is closer to $y = 0$, as regarding to the result as shown in Fig. 13(a). By increasing only the radius of the cylinder of the helix from 0.7 m to 1 m where $\delta_p = 0.4$, the symmetric shape appears (Fig. 13(c)). In this case the amplitude and the width of the Gaussian shape are greater than the amplitude and the width of the Gaussian shape as shown in Fig. 13(a). Now, by increasing the step's angle from $\delta_p = 0.4$ to $\delta_p = 0.8$ and also by increasing the radius of the cylinder of the helix from 0.7 m to 1 m, the amplitude and the width of the Gaussian shape (Fig. 13(d)) are greater than the amplitude and the width of the Gaussian shape in the previous cases. The symmetric shape (Gaussian shape) is shown in Fig. 13(d) where $\delta_p = 0.8$ and $R = 1\,\mathrm{m}$.

From the above results we can see that the output power transmission, the amplitude of the output power density ($|S_{av}|$), and the output Gaussian shape are improved by increasing the step's angle or the radius of the cylinder of the helix, in the cases of space curved waveguides. The output modal profile is greatly affected by small parameters of R and δ_p, (e.g., $R = 0.7\,\mathrm{m}$, and $\delta_p = 0.4$). For small values of the step's angle, the helical waveguide becomes a toroidal waveguide, where the radius of the curvature of the helix (ρ) can then be approximately by the radius of the cylinder (R). For small values of R (e.g., $R = 0.7\,\mathrm{m}$), the output shapes of the fields and the output power density ($|S_{av}|$) are far from a Gaussian shape, as shown in Fig. 12(a) and Fig. 13(a), for instance. The amplitude of the output power density is small (e.g., $(|S_{av}|) = 0.4\,\mathrm{W/m^2}$) as the radius of the cylinder is small (e.g., $R = 0.7\,\mathrm{m}$), and the output shape is far from a Gaussian shape, as shown in Fig. 13(a), for instance. The asymmetric output shape appears in this case, the width of the output Gaussian shape is smaller with regard to the width of the output Gaussian shape of the symmetric case (Fig. 13(d)).

This mode model enables us to understand the influence of the step's angle (δ_p) and the radius of the cylinder (R) on the output results (output power transmission, etc.). The output power transmission is improved by increasing the step's angle or by increasing the radius of the cylinder of the helix. The best results are obtained by increasing the value of δ_p and also by increasing the value of R. Thus, this model can be a useful tool to find the parameters (δ_p and R) which will give us the improved results (output power transmission, output power density, etc.) of a hollow waveguide in the cases of space curved waveguides, and for application in the medical and industrial fields.

5. CONCLUSIONS

The main objective was to generalize the method [16] from the curved dielectric waveguide (approximately a plane curve) with a circular cross-section to a helical waveguide (a space curved waveguide for an arbitrary value of the step's angle of the helix) with a circular cross-section. Another objective was to demonstrate the ability of the model to solve practical problems with inhomogeneous cross-section in the case of hollow waveguides. The generalized mode model with the two above objectives provides us a numerical tool for the calculation of the output fields, output power density, and output power transmission for an arbitrary value of the step's angle of the helix (δ_p), in the case of a hollow waveguide.

Three test-cases were demonstrated for small values of the step's angle. The first test-case was demonstrated for the straight waveguide ($R \to \infty$). The results of the output transverse components of the fields and the output power density (e.g., Fig. 7(a)) show the same behavior of the solutions as shown in the results of Ref. [16] for the TEM_{00} mode in excitation. The result of the output power density (Fig. 7(a)) was compared also to the result of the previous published experimental data [24] (see also in Fig. 7(b)). The comparison shows good agreement (a Gaussian shape) as expected, except for the secondary small propagation mode.

The second and third test-cases were demonstrated in the case of the toroidal dielectric waveguide. The second test-case was demonstrated (Fig. 8(a)) where the initial diameter (ID) is 1 mm (namely, small bore size). The output modal profile is greatly affected by the bending. The theoretical and experimental results (Figs. 8(a)–(b)) show that in addition to the main propagation mode, several other secondary modes and asymmetric shape appear. The amplitude of the output power density is small as the bending radius (R) is small, and the shape is far from a Gaussian shape. In the third test-case, the result of the output power transmission (Fig. 9) was compared to the experimental data [11]. Our theoretical model takes into account only the dielectric losses and the bending losses, in conjunction with the problem of the propagation through a curved waveguide. The experimental result (Fig. 8(b)) and the experimental result [11] take into account additional parameters (e.g., the roughnes of the internal wall of the waveguide) which are not taken into account theoretically. In spite of the differences, the comparisons show good agreements. For small values of the bending ($1/R$) in the case of small step's angle, the output power transmission is large and decreases with increasing the bending.

The results of the radius of curvature of the helix (ρ) as a function of $1/R$ and the results of the output power transmission of the helical waveguide as a function of $1/R$ are shown in Fig. 10 and in Fig. 11, respectively, where R is the radius of the cylinder. For an arbitrary value of R, the radius of curvature of the helix (ρ) and the output power transmission are large for large values of δ_p and decrease with decreasing the value of δ_p. On the other hand, for an arbitrary value of δ_p, the radius of curvature of the helix (ρ) and the output power transmission are large for large values of R and decrease with decreasing the value of R.

The results of the output power density as functions of the step's angle (δ_p) and the radius of the cylinder (R) are shown in Figs. 12(a)–(d). The output amplitude, the width of the Gaussian shape, and the shift of the central peak are shown in Figs. 13(a)–(d), in the same cross section of Figs. 12(a)–(d). In addition to the main propagation mode, several other secondary modes appear in Figs. 12(a) and 13(a), where $\delta_p = 0.4$ and $R = 0.7\,\mathrm{m}$, and the output modal profile is greatly affected in this case. By increasing only the step's angle or the radius of the cylinder of the helix, the amplitude of the output power density and the width of the Gaussian shape are greater and the output shape is changed from asymmetric shape to the symmetric shape. The best results in these examples are shown in Figs. 12(d) and 13(d), by increasing the value of δ_p and also by increasing the value of R.

This mode model enables us to understand the influence of the step's angle (δ_p) and the radius of the cylinder (R) on the output results (output power transmission, etc.). The output power transmission is improved by increasing the step's angle or by increasing the radius of the cylinder of the helix. The best results are obtained by increasing the value of δ_p and also by increasing the value of R. Thus, this model can be a useful tool to find the parameters (δ_p and R) which will give the improved results (output power transmission, output power density, etc.) of a hollow waveguide in the cases of space curved waveguides, and for application in the medical and industrial fields.

APPENDIX A.

By using the Serret-Frenet relations for a spatial curve, we can find the curvature (κ) and the torsion (τ) for each spatial curve that is characterized by $\theta = \text{const}$ and $r = \text{const}$ for each pair (r, θ) in the range. This is achieved by using the helical transformation introduced in equations (3a)–(3c).

The location vector for the helical transformation of the

coordinates (3a)–(3c) is given by

$$\begin{aligned}\boldsymbol{r} &= \Big((R + r\sin\theta)\cos(\phi_c) + r\sin(\delta_p)\cos\theta\sin(\phi_c)\Big)\hat{i} \\ &+ \Big((R + r\sin\theta)\sin(\phi_c) - r\sin(\delta_p)\cos\theta\cos(\phi_c)\Big)\hat{j} \\ &+ \Big(r\cos\theta\cos(\delta_p) + R\phi_c\tan(\delta_p)\Big)\hat{k}, \end{aligned} \tag{A1}$$

where $\phi_c = (\zeta/R)\cos(\delta_p)$, R is the radius of the cylinder, and (r, θ) are the parameters of the cross-section.

The tangent vector is given by $\boldsymbol{T} = (d\boldsymbol{r}/d\zeta) = (d\boldsymbol{r}/d\phi_c)/(d\zeta/d\phi_c)$. The normal vector is given by $\boldsymbol{N} = (1/\kappa)(d\boldsymbol{T}/d\zeta)$, and the binormal vector is given by $\boldsymbol{B} = \boldsymbol{T} \times \boldsymbol{N}$.

The rate of the change of the tangent vector related to the parameter ζ measurses the curvature, and is given by $d\boldsymbol{T}/d\zeta = (d\boldsymbol{T}/d\phi_c)/(d\zeta/d\phi_c)$.

The curvature of the helix is constant for constant values of the radius of the cylinder (R), the step's angle (δ_p) and the parameters (r, θ) of the cross-section. The curvature is given by the first Serret-Frenet equation of a curve $r(\zeta)$ in the space according to $d\boldsymbol{T}/d\zeta = \kappa\boldsymbol{N}$. Thus, the curvature is

$$\kappa = \left|\frac{d\boldsymbol{T}}{d\zeta}\right| = \frac{1 + C_t}{R(1 + \tan^2(\delta_p) + C_t)}, \tag{A2}$$

where

$$C_t = \frac{r^2}{R^2}\sin^2\theta + 2\frac{r}{R}\sin\theta + \frac{r^2}{R^2}\sin^2(\delta_p)\cos^2\theta,$$

and the radius of curvature is given by $\rho = 1/\ \kappa$.

The rate of the change of the binormal vector related to the parameter ζ measurses the torsion, and is given by $d\boldsymbol{B}/d\zeta = (d\boldsymbol{B}/d\phi_c)/(d\zeta/d\phi_c)$.

The torsion of the helix is constant for constant values of the radius of the cylinder (R), the step's angle (δ_p) and the parameters (r, θ) of the cross-section. The torsion is given by the second Serret-Frenet equation of a curve $r(\zeta)$ in the space according to $d\boldsymbol{B}/d\zeta = -\tau\boldsymbol{N}$. Thus, the torsion is

$$\tau = \left|\frac{d\boldsymbol{B}}{d\zeta}\right| = \frac{\tan\delta_p}{R(1 + \tan^2(\delta_p) + C_t)}, \tag{A3}$$

where C_t is given above, and the radius of torsion is given by $\sigma = 1/\tau$.

APPENDIX B.

The elements of the matrices ($G_{00}^{(1)mm'}$, etc.) are given by:

$$
\begin{aligned}
G_{00}^{(1)mm'} &= \int_0^a J_1\left(P_{1m'}\frac{r}{a}\right)J_1\left(P_{1m}\frac{r}{a}\right)rdr\delta_{1n},\\
G_{01}^{(1)mm'} &= \int_0^a g(r)J_1\left(P_{1m'}\frac{r}{a}\right)J_1\left(P_{1m}\frac{r}{a}\right)rdr\delta_{1n},\\
G_{02}^{(1)mm'} &= \int_0^a J_1\left(P_{1m'}\frac{r}{a}\right)J_1\left(P_{1m}\frac{r}{a}\right)r^3dr\delta_{1n},\\
G_{03}^{(1)mm'} &= \int_0^a g(r)J_1\left(P_{1m'}\frac{r}{a}\right)J_1\left(P_{1m}\frac{r}{a}\right)r^3dr\delta_{1n},\\
G_{04}^{(1)mm'} &= \int_0^a g^2(r)J_1\left(P_{1m'}\frac{r}{a}\right)J_1\left(P_{1m}\frac{r}{a}\right)r^3dr\delta_{1n},\\
G_{05}^{(1)mm'} &= \int_0^a k^2g(r)J_1\left(P_{1m'}\frac{r}{a}\right)J_1\left(P_{1m}\frac{r}{a}\right)rdr\delta_{1n},\\
G_{06}^{(1)mm'} &= \int_0^a J_1\left(P_{1m'}\frac{r}{a}\right)J_1\left(P_{1m}\frac{r}{a}\right)r^5dr\delta_{1n},\\
G_{07}^{(1)mm'} &= \int_0^a g(r)J_1\left(P_{1m'}\frac{r}{a}\right)J_1\left(P_{1m}\frac{r}{a}\right)r^5dr\delta_{1n},\\
G_{08}^{(1)mm'} &= \int_0^a g_r\left(\frac{P_{1m'}}{a}\right)J_1{}'\left(P_{1m'}\frac{r}{a}\right)J_1\left(P_{1m}\frac{r}{a}\right)rdr,\\
G_{09}^{(1)mm'} &= \int_0^a g_rJ_1\left(P_{1m'}\frac{r}{a}\right)J_1\left(P_{1m}\frac{r}{a}\right)r^2dr\delta_{1n},\\
G_{10}^{(1)mm'} &= \int_0^a J_1{}'\left(\frac{P_{1m'}r}{a}\right)J_1\left(P_{1m}\frac{r}{a}\right)r^2dr\delta_{1n},\\
G_{11}^{(1)mm'} &= \int_0^a g_rJ_1{}'\left(\frac{P_{1m'}r}{a}\right)J_1\left(P_{1m}\frac{r}{a}\right)r^3dr\delta_{1n},\\
G_{12}^{(1)mm'} &= \int_0^a g^2(r)J_1\left(P_{1m'}\frac{r}{a}\right)J_1\left(P_{1m}\frac{r}{a}\right)r^5dr\delta_{1n},\\
G_{13}^{(1)mm'} &= \int_0^a g_rJ_1{}'\left(\frac{p_{1m'}'r}{a}\right)J_1\left(P_{1m}\frac{r}{a}\right)dr\delta_{1n},
\end{aligned}
$$

$$G_{14}^{(1)mm'} = \int_0^a g_r J_1\left(\frac{p'_{1m'}r}{a}\right) J_1\left(P_{1m}\frac{r}{a}\right) r^2 dr\delta_{1n},$$

$$G_{15}^{(1)mm'} = \int_0^a J_1\left(P'_{1m'}\frac{r}{a}\right) J_1\left(P_{1m}\frac{r}{a}\right) r dr\delta_{1n},$$

$$G_{16}^{(1)mm'} = \int_0^a J_1{}'\left(\frac{P'_{1m'}r}{a}\right) J_1\left(P_{1m}\frac{r}{a}\right) r^2 dr\delta_{1n}.$$

Similarly, the remaining elements are obtained. The coefficients are obtained directly from the algebraic system of equations (18a)–(18d) and are expressed as functions in s-plane. Similarly, the other coefficients are obtained.

APPENDIX C.

The other transverse components of the fields are finally expressed in a form of *transfer matrix functions* as follows

$$\begin{aligned}
E_\theta(r,\theta,\zeta) = {} & E_{\theta 0}^{+}(r)e^{-jkh_\zeta\zeta} + \frac{j\omega\mu_0}{R}h_\zeta \sin\theta\cos\theta\cos^2(\delta_p)\sum_{m'} C_{S1}^{m'}(\zeta)J_1(\psi) \\
& + \frac{j\omega\mu_0}{R}h_\zeta \sin^2\theta\cos^2(\delta_p)\sum_{m'} D_{S1}^{m'}(\zeta)J_1(\psi) \\
& + j\omega\mu_0 h_\zeta^2 \cos\theta \sum_{m'} C_{S1}^{m'}(\zeta)\frac{dJ_1}{dr}(\psi) \\
& + j\omega\mu_0 h_\zeta^2 \sin\theta \sum_{m'} D_{S1}^{m'}(\zeta)\frac{dJ_1}{dr}(\psi) \\
& + \frac{1}{R}\cos^2\theta\cos^2(\delta_p)\sum_{m'} A_{S2}^{m'}(\zeta)J_1(\xi) \\
& + \frac{1}{R}\sin\theta\cos\theta\cos^2(\delta_p)\sum_{m'} B_{S2}^{m'}(\zeta)J_1(\xi) \\
& - \frac{1}{r}h_\zeta \sin\theta\sum_{m'} A_{S2}^{m'}(\zeta)J_1(\xi) + \frac{1}{r}h_\zeta\cos\theta\sum_{m'} B_{S2}^{m'}(\zeta)J_1(\xi),
\end{aligned} \tag{C1}$$

$$
\begin{aligned}
H_r(r,\theta,\zeta) = {} & H_{r0}^{+}(r)e^{-jkh_\zeta\zeta} + \frac{j\omega\epsilon}{R}h_\zeta\cos^2\theta\cos^2(\delta_p)\sum_{m'}A_{S1}^{m'}(\zeta)J_1(\xi) \\
& + \frac{j\omega\epsilon}{R}h_\zeta\sin\theta\cos\theta\cos^2(\delta_p)\sum_{m'}B_{S1}^{m'}(\zeta)J_1(\xi) \\
& - \frac{j\omega\epsilon}{r}h_\zeta^2\sin\theta\sum_{m'}A_{S1}^{m'}(\zeta)J_1(\xi) \\
& + \frac{j\omega\epsilon}{r}h_\zeta^2\cos\theta\sum_{m'}B_{S1}^{m'}(\zeta)J_1(\xi) \\
& + \frac{1}{R}\sin\theta\cos\theta\cos^2(\delta_p)\sum_{m'}C_{S2}^{m'}(\zeta)J_1(\psi) \\
& + \frac{1}{R}\sin^2\theta\cos^2(\delta_p)\sum_{m'}D_{S2}^{m'}(\zeta)J_1(\psi) \\
& + h_\zeta\cos\theta\sum_{m'}C_{S2}^{m'}(\zeta)\frac{dJ_1}{dr}(\psi) + h_\zeta\sin\theta\sum_{m'}D_{S2}^{m'}(\zeta)\frac{dJ_1}{dr}(\psi),
\end{aligned}
\tag{C2}
$$

$$
\begin{aligned}
H_\theta(r,\theta,\zeta) = {} & H_{\theta0}^{+}(r)e^{-jkh_\zeta\zeta} - \frac{j\omega\epsilon}{R}h_\zeta\sin\theta\cos\theta\cos^2(\delta_p)\sum_{m'}A_{S1}^{m'}(\zeta)J_1(\xi) \\
& - \frac{j\omega\epsilon}{R}h_\zeta\sin^2\theta\cos^2(\delta_p)\sum_{m'}B_{S1}^{m'}(\zeta)J_1(\xi) \\
& - j\omega\epsilon h_\zeta^2\cos\theta\sum_{m'}A_{S1}^{m'}(\zeta)\frac{dJ_1}{dr}(\xi) \\
& - j\omega\epsilon h_\zeta^2\sin\theta\sum_{m'}B_{S1}^{m'}(\zeta)\frac{dJ_1}{dr}(\xi) \\
& + \frac{1}{R}\cos^2\theta\cos^2(\delta_p)\sum_{m'}C_{S2}^{m'}(\zeta)J_1(\psi) \\
& + \frac{1}{R}\sin\theta\cos\theta\cos^2(\delta_p)\sum_{m'}D_{S2}^{m'}(\zeta)J_1(\psi) \\
& - \frac{1}{r}h_\zeta\sin\theta\sum_{m'}C_{S2}^{m'}(\zeta)J_1(\psi) + \frac{1}{r}h_\zeta\cos\theta\sum_{m'}D_{S2}^{m'}(\zeta)J_1(\psi).
\end{aligned}
\tag{C3}
$$

REFERENCES

1. Harrington, J. A. and Y. Matsuura, "Review of hollow waveguide technology," *Biomedical Optoelectronic Instrumentation*, A. Katzir, J. A. Harrington, and D. M. Harris (eds.), *SPIE*, Vol. 2396, 4–14, 1995.
2. Harrington, J. A., "A review of IR transmitting, hollow waveguides," *Fiber and Integrated Optics*, Vol. 19, 211–228, 2000.
3. Marcatili, E. A. J. and R. A. Schmeltzer, "Hollow metallic and dielectric waveguides for long distance optical transmission and lasers," *Bell Syst. Tech. J.*, Vol. 43, 1783–1809, 1964.
4. Marhic, M. E., "Mode-coupling analysis of bending losses in IR metallic waveguides," *Appl. Opt.*, Vol. 20, 3436–3441, 1981.
5. Miyagi, M., K. Harada, and S. Kawakami, "Wave propagation and attenuation in the general class of circular hollow waveguides with uniform curvature," *IEEE Trans. Microwave Theory Tech.*, Vol. MTT-32, 513–521, 1984.
6. Croitoru, N., E. Goldenberg, D. Mendlovic, S. Ruschin, and N. Shamir, "Infrared chalcogenide tube waveguides," *SPIE*, Vol. 618, 140–145, 1986.
7. Melloni, A., F. Carniel, R. Costa, and M. Martinelli, "Determination of bend mode characteristics in dielectric waveguides," *J. Lightwave Technol.*, Vol. 19, 571–577, 2001.
8. Bienstman, P., M. Roelens, M. Vanwolleghem, and R. Baets, "Calculation of bending losses in dielectric waveguides using eigenmode expansion and perfectly matched layers," *IEEE Photon. Technol. Lett.*, Vol. 14, 164–166, 2002.
9. Mejias, P. M., "Light propagation through inhomogeneous media with radial refractive index: application to thermal blooming," *Appl. Opt.*, Vol. 20, 4287–4295, 1981.
10. Mendlovic, D., E. Goldenberg, S. Ruschin, J. Dror, and N. Croitoru, "Ray model for transmission of metallic-dielectric hollow bent cylindrical waveguides," *Appl. Opt.*, Vol. 28, 708–712, 1989.
11. Morhaim, O., D. Mendlovic, I. Gannot, J. Dror, and N. Croitoru, "Ray model for transmission of infrared radiation through multibent cylindrical waveguides," *Opt. Eng.*, Vol. 30, 1886–1891, 1991.
12. Kark, K. W., "Perturbation analysis of electromagnetic eigenmodes in toroidal waveguides," *IEEE Trans. Microwave Theory Tech.*, Vol. MTT-39, 631–637, 1991.

13. Lewin, L., D. C. Chang, and E. F. Kuester, *Electromagnetic Waves and Curved Structures*, Chap. 6, 58–68, Peter Peregrinus Ltd., London, 1977.
14. Ghosh, S., P. K. Jain, and B. N. Basu, "Fast-wave analysis of an inhomogeneously-loaded helix enclosed in a cylindrical waveguide," *Progress in Electromagnetics Research*, PIER 18, 19–43, 1998.
15. Kumar, D. and O. N. Singh II, "Elliptical and circular step-index fibers with conducting helical windings on the core-cladding boundaries for different winding pitch angles — A comparative modal dispersion analysis," *Progress in Electromagnetics Research*, PIER 52, 1–21, 2005.
16. Menachem, Z., N. Croitoru, and J. Aboudi, "Improved mode model for infrared wave propagation in a toroidal dielectric waveguide and applications," *Opt. Eng.*, Vol. 41, 2169–2180, 2002.
17. Collin, R. E., *Foundation for Microwave Engineering*, McGraw-Hill, New York, 1996.
18. Yariv, A., *Optical Electronics*, 3rd ed., Holt-Saunders Int. Editions, 1985.
19. Baden Fuller, A. J., *Microwaves*, Chap. 5, 118–120, A. Wheaton and Co. Ltd, Pergamon Press, Oxford, 1969.
20. Olver, F. W. J., *Royal Society Mathematical Tables, Zeros and Associated Values*, 2–30, University Press Cambridge, 1960.
21. Jahnke, E. and F. Emde, *Tables of Functions with Formulae and Curves*, Chap. 8, 166, Dover publications, New York, 1945.
22. The Numerical Algorithms Group (NAG) Ltd., Wilkinson House, Oxford, U.K.
23. Menachem, Z., "Wave propagation in a curved waveguide with arbitrary dielectric transverse profiles," *Journal of Electromagnetic Waves and Applications*, Vol. 17, 1423–1424, 2003, and *Progress in Electromagnetics Research*, PIER 42, 173–192, 2003.
24. Croitoru, N., A. Inberg, M. Oksman, and M. Ben-David, "Hollow silica, metal and plastic waveguides for hard tissue medical applications," *SPIE*, Vol. 2977, 30–35, 1997.